PCCP

PAPER

View Article Online
View Journal | View Issue

Cite this: *Phys. Chem. Chem. Phys.*, 2026, **28**, 6884

Investigating the kinetics of spin-crossover transitions using Raman spectroscopy

Gérald Kämmerer, [a] Lea Kämmerer, [a] Stephan Sleziona, [a] Senthil Kumar Kuppusamy, [b] Mario Ruben, [bcd] Marika Schleberger, [a] Heiko Wende [a] and Peter Kratzer *[a]

The room-temperature spin-crossover iron(II) complex Fe(1-bpp-$COOC_2H_5$)$_2$(BF_4)$_2$$CH_3CN$ exhibits reversible switching between the low-spin and high-spin states. The observation of coexisting spin domains within polycrystalline samples of Fe(1-bpp-$COOC_2H_5$)$_2$(BF_4)$_2$$CH_3CN$ allows for real-time video recording of domain boundary propagation under an optical microscope. Quantitative analysis of this motion provides valuable information regarding the phenomenological transition involved in the spin-state switching process. To elucidate the intricate dynamics of this spin transition, a synergistic approach combining temperature-dependent Raman spectroscopy with *ab initio* computational methods is employed. Within this investigation, a comprehensive classification of Raman vibrational modes has been achieved, categorizing them based on their spin-state dependence and vibrational characteristics, symmetries, including stretching, bending, and tilting motions. Notably, low-frequency Raman modes associated with the iron center and its nitrogen ligand environment provide crucial insights into the local coordination and its role in the spin-crossover mechanism. This work reveals distinct spin-state-induced structural changes, including bond stretching and softening, which manifest as unique spectroscopic fingerprints for each spin state.

Received 18th November 2025,
Accepted 20th February 2026

DOI: 10.1039/d5cp04473a

rsc.li/pccp

1 Introduction

Spin-crossover (SCO) molecules are a class of molecular materials exhibiting a bi-stable spin transition between low-spin (LS, $S = 0$) and high-spin (HS, $S = 2$) states. This transition, induced by external stimuli such as temperature, pressure, X-rays, static electric or magnetic fields, or inclusion of guest molecules, is accompanied by significant alterations in their electronic, optical and geometric properties.[1–11] The SCO phenomenon for a single molecule centers on the Fe(II) ion, a transition metal with partially filled 3d orbitals.[12–14] Ligand coordination induces splitting of the Fe 3d orbitals into e_g and t_{2g} sets. Temperature-induced transitions from the diamagnetic low-spin state (LS, $S = 0$) to the paramagnetic high-spin state (HS, $S = 2$) are accompanied by a decrease in ligand field strength (10 Dq) and an approximate 10% elongation of Fe–N bond lengths[15–17] (see Fig. 1). Notably, N–N or C–C bond lengths are minimally affected by the spin transition. For practical applications, SCO complexes should exhibit abrupt spin-state switching with broad thermal hysteresis around room temperature and potential color changes.[1–8,10,11,18–21] Recent synthesis of crystalline samples with the complex Fe(1-bpp-$COOC_2H_5$)$_2$,[18] containing two BF_4^- counter-ions and one CH_3CN solvent molecule per unit cell, demonstrates spin-state switching near room temperature with pronounced hysteresis. This switching, occurring near $T_\uparrow$ = 321 K and accompanied by a color change from gray (LS) to orange (HS) (see Fig. 3, right part), is consistent with observations in other SCO materials.[22–25] It is accompanied by a broad hysteresis making our SCO a promising candidate for applications in molecular switching and nanoelectronics devices, including light-emitting diodes.[3,26–28]

To lay the ground for the work presented in this paper, we summarize observations reported previously on similar samples. It is well known that the spin-state transition is reflected in the average Fe–N bond length, as corroborated by experimental X-ray diffraction (XRD) data[9,18] and *ab initio* calculations, see Fig. 1 for detailed values. Moreover, the XRD data also reveals that the monoclinic cells of the LS and HS phases differ in both shape and volume, with the HS phase exhibiting a 2%

[a] *Faculty of Physics and Center for Nanointegration Duisburg-Essen (CENIDE), University Duisburg-Essen, Lotharstraße 1, 47057 Duisburg, Germany. E-mail: gerald.kaemmerer@uni-due.de, peter.kratzer@uni-due.de*
[b] *Institute of Quantum Materials and Technologies (IQMT), Karlsruhe Institute of Technology (KIT), Kaiserstraße 12, 76131 Karlsruhe, Germany*
[c] *Institute of Nanotechnology (IMT), Karlsruhe Institute of Technology (KIT), Kaiserstraße 12, 76131 Karlsruhe, Germany*
[d] *Centre Européen de Sciences Quantiques (CESQ), Institut de Science et d'Ingénierie, Supramoléculaires (ISIS), 8 allée Gaspard Monge, BP 70028, 67083 Strasbourg Cedex, France*

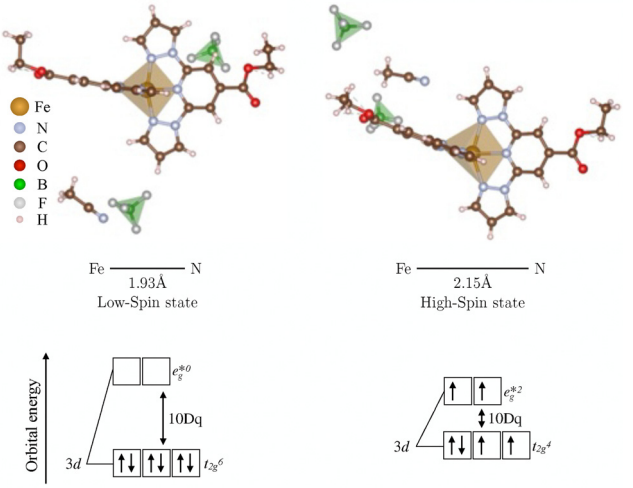

Fig. 1 Top Panel: The crystallographic structure of Fe(1-bpp-$COOC_2H_5$)$_2$-(BF_4)$_2$$CH_3CN$ is presented, highlighting the average Fe–N bond distances calculated using density functional theory (DFT): the panel illustrates the spin-state-dependent conformational changes of the ethyl (C_2H_5) substituents, which adopt an out-of-plane configuration in the low-spin (LS) state and an in-plane configuration in the high-spin (HS) state. Additionally, the spatial position of the BF_4^- counter-anions and the CH_3CN solvent molecule is shown, reflecting their respective position in the LS and HS states. Bottom Panel: A schematic energy level diagram illustrates the splitting of the Fe(II) 3d orbitals in a ligand field. The diagram demonstrates the formation of the t_{2g} and antibonding e_g* in the O_h representation, providing a simplified model for understanding the electronic transitions responsible for the thermally induced spin-state crossover in this complex.

volume increase. This hysteretic behavior is associated with a phase coexistence observable in optical microscopy due to the color change between the two phases. While the switching of individual molecules occur on the femtosecond time scale (*e.g.*,[10,29–32]), the much slower process of the growth of phase domains could provide further insight into the switching kinetics. Monitoring the speed of the domain boundary between LS and HS phases during hysteresis is an obvious way to access these kinetics.

From the experimental perspective, we employ a combination of techniques: optical microscopy provides insight into macro- and mesoscopic strain within the sample and its effect on crystal integrity, while Raman spectroscopy probes the motion of individual molecules and their interactions at the sub-molecular level. Raman spectroscopy, a non-destructive technique, offers valuable insight into the molecular structural evolution during spin-state switching.[19] It has been demonstrated already that this method allows one to distinguish between LS and HS states, as exemplified by the pyridine ring breathing mode near 1020 cm^{-1}, which exhibits significant shifts due to Fe–N bond elongation upon LS-to-HS transition.[33,34]

In the present work, we study polycrystalline material. In these samples, the LS and HS states show up as separate phase domains, growing, and shrinking as temperature is swept through the thermal hysteresis loop. The transition behavior depends on the material history, and the so-called "self-grinding" phenomenon[35] is observed. We carried out a temperature-dependent analysis of the phase boundary motion. Simultaneously, the microscopic changes were monitored *via* Raman spectroscopy. This poses the question of how exactly the material's properties in the microstructure of this polycrystalline material and at the molecular level interact when the spin state is switched. Combining Raman spectroscopy with *ab initio* calculations enables the development of a unique structural fingerprint for Fe(1-bpp-$COOC_2H_5$)$_2$(BF_4)$_2$$CH_3CN$, similar to the approach used by Devid[36] for other SCO complexes.[36–41] By comparing Raman data sets with *ab initio* calculations, the typical spectral features can be classified, and the specific differences between LS/HS modes can be investigated, allowing a clear identification of distinct vibrational modes according to the atomic species in the bonding.[38,40]

2 Experimental and theoretical methods

2.1 Sample preparation and characterization

The preparation and characterization of our samples has been described previously,[18] and here we just summarize the information relevant to us. Our polycrystalline sample (several hundred μm^3, $\rho \approx 1.537$ g cm^{-3}) crystallizes in the LS state within the monoclinic space group $P2_1/c$ (CCDC 1560719). Upon transition to the HS state, a crystallographic phase transformation to space group $P2_1/n$ (CCDC 2330939) occurs. This phase transition involves a shearing of the cell (estimated from XRD[18]), resulting in a restructuring of the crystal lattice that is closely related to the spin-state transition and adjustments in molecular packing. The shearing and increasing of the unit cell causes a translation and rotation of the SCO molecules, counter-anions, and solvents. The compound, Fe(1-bpp-$COOC_2H_5$)$_2$(BF_4)$_2$$CH_3CN$, features a central iron(II) ion (Fe^{2+}) coordinated by two tridentate 2,6-di(pyrazol-1-yl)-pyridine (1-bpp) ligands functionalized with ethyl ester groups (–$COOC_2H_5$). The resulting cationic complex is charge-balanced by two tetrafluoroborate anions (BF_4^-) and solvated in acetonitrile (CH_3CN), indicative of its crystallization state (molecular and solvent/anion structures in Fig. 1). Taking the tilting of the ethyl ester group into account, the molecule has a symmetry of C_{2v}. As reported in Kuppusamy *et al.* (2019),[18] the complex exhibits a distorted geometry in the HS state, with a *trans*-N(pyridine)-Fe-N(pyridine) angle of approximately 158.83° (LS: 178.91°), deviating from idealized octahedral symmetry.

2.2 Temperature-dependent Raman spectroscopy

Raman spectroscopy was performed using a WITec alpha300RA confocal Raman microscope with a Linkam THMS350EV vacuum stage. To minimize thermal artifacts, samples were maintained in a nitrogen atmosphere and cryogenically cooled with liquid nitrogen. Raman spectra were taken at various temperatures with a 532 nm laser at 0.5 mW for excitation, and a ZeissLS Epiplan-Neofluar 50× objective (NA 0.55) for laser focusing and optical image acquisition. Ultralow frequency modes (down to 10 cm^{-1}) were resolved using a

RayShield filter. Spectral peak positions were determined by fitting the data with Gaussian functions. Mode identification in this paper between experiment and simulation was based primarily on frequency shifts and the selection of the modes is based on the relative intensity variations in the experimental measurement. Raman intensities calculated within the non-resonant approximation (not presented here) showed limited correlation with experimental results and are therefore not further discussed. To elucidate switching dynamics and time-scales, video recordings were acquired during Raman measurements. These recordings enabled analysis of dynamic features while from temperature-dependent Raman spectroscopy we can identify spectral features for the HS and LS state, seen Fig. 3.

2.3 Investigation of the phase boundary movements

Video recordings were analyzed using self-written Python scripts to identify the phase transition region, extract propagation times, and estimate the phase transition boundary velocity (see Table 3). The boundary was determined using an edge detection algorithm, combined with gradient color intensity analysis and Haar-like feature detection (Histogram of Oriented Gradients, HOG[42]). Variations in video focus occasionally complicated velocity determination; these were mitigated through gradient interpolation, enabling error estimation. This approach facilitated the study of intermolecular coupling dynamics during heating and cooling (see Fig. 7). Various heating and cooling rates and temperature ranges were investigated. However, morphological changes (the "self-grinding" phenomenon[35]), along with stress-induced strain that introduced cracks, grains, and sometimes caused parts to chip off, significantly complicating rate determination during cooling, necessitating interpolation and dynamic boundary identification to estimate the cooling velocity. Despite these complications, the boundary velocity remained largely unchanged, although the material's history was important for determining the state and the transitions.

2.4 Computational method

Density functional theory (DFT) with the finite displacement method was used to compute molecular vibrational spectra. Given the computational complexity associated with the large number of vibrational modes (exceeding 201), the Perdew–Burke–Ernzerhof (PBE) functional[43] was selected, based on its demonstrated efficacy in similar investigations.[44] DFT calculations were performed using the FHI-aims code,[45] an all-electron code with numerically defined atom-centered basis functions, employing the tight basis set (tier 2), van der Waals correction,[46] and the atomic zero-order regular approximation (ZORA).[47] This method is known for its efficiency in DFT and Raman mode calculations, albeit with substantial computational requirements. For the calculation, we used the standard parameters of a full geometry relaxation with the *BFGS* algorithm with and without periodic boundary conditions and a threshold on the forces on atoms of 5×10^{-4} eV Å^{-1} while in the self-consistency cycle forces were converged to 2×10^{-6} eV Å^{-1} and electronic density changes were less than 2×10^{-7} ea$_0^{-3}$. Subsequent to the converged non-periodic calculation, we used the given core script get_vibrations.py of FHI-aims to calculate (set δ = 0.0025 Å) the vibrational modes and checked for any unstable modes. Raman frequencies were determined for both spin states. Initial geometries from X-ray diffraction data published in the literature[18] were geometrically optimized for both HS and LS complexes, considering periodic and free-standing boundary conditions. The free-standing approach provided sufficient accuracy for simulating Raman modes and identifying modes associated with iron-nitrogen or (1-bpp-$COOC_2H_5$)$_2$ unit interactions during spin-state switching, compared to periodic calculations.[48]

Calculations were performed on both the full (including counter-anions and lattice solvent) and the minimal (charged Fe(1-bpp-$COOC_2H_5$)$^{2+}$ complex, excluding the smaller molecules) molecular configurations. Comparative analysis showed that including counter-anions and lattice solvent had a negligible effect (0.2% difference) on the calculated bond lengths (Fe–N bonds to pyridine and pyrazole 1.88 Å and 1.96 Å, respectively) and bond angles (179° and 161°) in the LS state, consistent with findings in a different material by Lawson Daku.[49]

3 Results

3.1 Temperature-dependent Raman spectra

The range for temperatures of interest is determined from taking a thermal hysteresis curve, as shown in Fig. 2. The temperature-dependent Raman spectra acquired during such a thermal cycle are shown in Fig. 3, encompassing heating from 300 K to 340 K and subsequent cooling to 220 K, at discrete temperature points (300 K, 318 K, 340 K, 300 K, 270 K, and 220 K), as marked in the hysteresis plot in Fig. 2. Concurrent optical observations, documented as images and for the domain investigation as video, are presented alongside the corresponding Raman spectra (temporally resolved Raman spectra recording was not feasible).

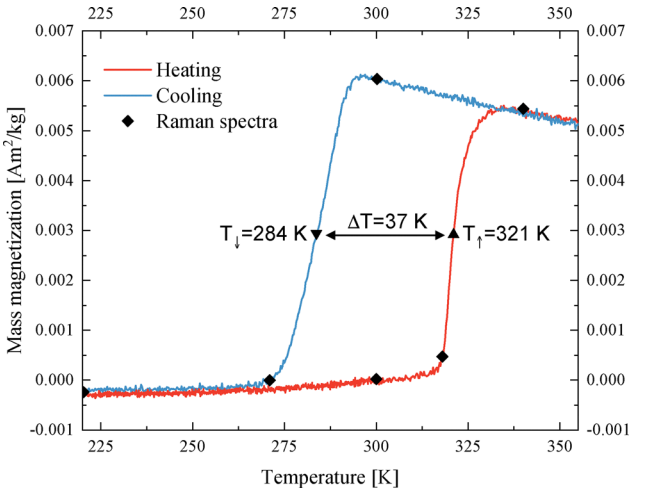

Fig. 2 Temperature-dependent thermal hysteresis in the temperature regime of 220 to 350 K with a broad hysteresis of 37 K. The symbols mark the temperatures of the Raman measurements shown in the Fig. 3.

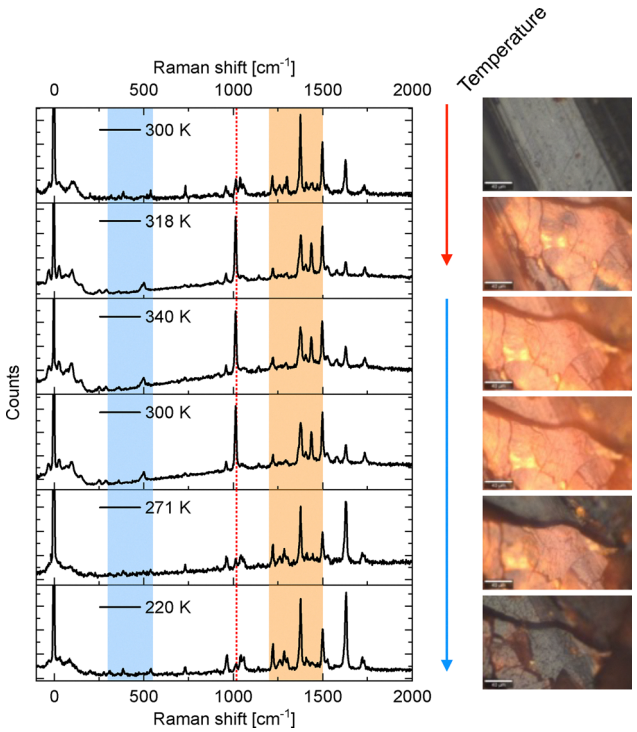

Fig. 3 Raman spectra measured at different temperatures with the corresponding optical microscopy images: The left panel of Fig. 3 displays six Raman spectra recorded at 300 K, 318 K, 340 K, 300 K, 270 K, and 220 K, spanning a Raman shift range from 0 to 2000 cm^{-1}. Spectral key features appear and disappear depending on the temperature, particularly in the regions between 300–550 cm^{-1} (colored blue), 1200–1500 cm^{-1} (colored orange), and most prominently around 1017 cm^{-1} (dashed red). These features reflect changes in the vibrational modes of the sample (see Section 3.1). The right panel of Fig. 3 shows the corresponding optical microscope images, revealing a reversible color change associated with the spin state of the sample. At lower temperatures, the material exhibits a grayish-brown hue, corresponding to the low-spin (LS) state. Upon heating, the sample transitions into the high-spin (HS) state, accompanied by an orange-yellow coloration. Cooling the sample leads to a return to the LS state and its original grayish-brown appearance, consistent with the behavior observed in the videos. Additionally, in the intermediate temperature range between 318 K and 270 K, a faint luminescence was observed, resulting in a slight glooming effect in the microscope images and a broad background in the Raman measurements.

Analysis of the Raman spectra reveals several noteworthy features. Adjacent to the Rayleigh line (0 cm^{-1}), a low-intensity feature is observed, which exhibits a significant increase in intensity in the HS state. These low modes will be further discussed in the context of vibrations with a substantial iron contribution. Bands around 50 cm^{-1} up to 500 cm^{-1} are anticipated to be crucial for understanding the coupling of the iron between the ligands, as will be discussed later.

A prominent spectral feature is observed around 1000 cm^{-1}, displaying a marked change in intensity and appearing distinctly in the HS state while diminishing upon cooling. This mode is identified as pyridine ring breathing, coupled from one ligand to the other by the iron center (*cf.* Fig. 6 top row). A neighboring peak exhibits an inverse trend, decreasing in intensity as the 1000 cm^{-1} peak emerges. In the spectral region between 1100 and 1300 cm^{-1}, several features present in the LS state show a reduction in intensity in the HS state related to the structural change of the complex.

The broad spectral range between 1350 and 1700 cm^{-1} exhibits both an increase in overall intensity and a shift in the frequencies of individual peaks upon the transition to the HS state. Conversely, the Raman band observed around 1750 cm^{-1} remains largely unaffected by the spin state switching, suggesting its origin in a functional group of the molecule that is not directly involved in the electronic transition, which we can see in the mode assignment and in the Tables 1 and 2. For a further investigation, we need to assign the modes in a detailed comparison like in the Fig. 4 to understand the iron/bond interaction in the different spin states.

3.2 Vibrational mode assignment

For the present research, we are guided by the question of how the spin state of Fe is reflected in the pertaining spectra, in other words, whether there are 'fingerprints' in the spectra that allow one to conclude on the spin state of an individual Fe complex in the crystal. The Raman spectrometer used enables us to examine the low-frequency spectral range (<600 cm^{-1}), where modes involving significant Fe motion are expected. While high-frequency modes are not expected to involve Fe displacements due to the large atomic mass of Fe, even small Fe motions can mediate vibrational coupling between modes with displacements in both ligands.

The classification of the Raman-active vibrational modes starts from the experimentally identified peaks in the highly resolved Raman spectra shown in Fig. 4. From the overall 201 calculated vibrational modes, only those are reported in the Tables 1 and 2 for which a corresponding experimental mode could be identified. To establish a one-to-one correspondence between vibrational modes in the LS and HS states, a combined methodology was implemented, encompassing classification, symmetry classification, and density-based spatial clustering of applications with noise (DBSCAN)[50] on atomic displacements. The grouping of the modes was accomplished through a symmetry-based approach, wherein modes were assigned by visual inspection according to their closest possible symmetry. If we restrict ourselves to the Fe atoms and its six N neighbors, the complex has an approximate symmetry of D_{2d} (see Fig. 5). It contains a two-fold rotational axis C_2 and C_2' and two combined mirror-plus-rotation symmetry operations. In the following, the characterization as ''antisymmetric'' or ''symmetric'' refers to the parity of the vibrational displacements with respect to the latter two operations.

3.2.1. Low-mode range. Of particular interest is the classification of the modes in A_1, B_2, where displacements are distributed over both ligands and split into modes with in-phase and out-of-phase motion of the atoms. The magnitude of this splitting reflects the vibrational coupling strength, which depends on the Fe–N bonding strength, and thus on the Fe spin state. We expect a stronger splitting within the E representation in the LS state compared to the HS state.

Table 1 Vibrational modes of the complex Fe(1-bpp-$COOC_2H_5$)$_2$(BF_4)$_2$$CH_3CN$ in powder form below 1215 cm^{-1} for both the low-spin (LS) and high-spin (HS) states, using both experimental (exp.) methods and DFT calculations of a charged complex without counter-ions with the PBE functional (calc.). The calculations yielded multiple/degenerate (deg.) modes. Here, "Antisym." and "Sym." indicate whether the mode is antisymmetric or symmetric with respect to the mirror planes in Fig. 5

	Vibrational modes in [cm^{-1}]						
No.	LS_{exp}	LS_{calc}	HS_{exp}	HS_{calc}	Deg.	Sym.	Description
1	30	27.9	27	24.1	Deg. (2)	E	Bending of the ligands
2	99	104.9	95	104.4	Deg. (2)	E	Tilting pyridine, pyrazole rings
3	—	162.9	147	139.0	Non-Deg.	B_2	Iron mode, tilting pyrazole rings
4	205	210.6	—	233.7	Non-Deg.	A_1	Tilting pyridine, pyrazole rings, iron mode
5	—	262.6, 262.9	257	261.9, 262.3	Deg. (2)	E	Ethyl group tilting
6	310	315.7, 308.7, 315.8	296	279.8, 266.4, 288.02	Deg. (3)	—	Iron mode, bending C–N bond
7	361	350.12	364	289.0	Non-Deg.	B_2	Antisym. N–Fe bond stretching
8	387	375.9, 377.2	—	336.0, 336.3	Deg. (2)	E	Antisym. and sym. N–Fe bond stretching
9	—	523.1, 539.2	505	507.7, 509.1	Deg. (2)	E	Tilting pyridine ring
10	539	521.0, 521.3	—	585.1, 585.2	Deg. (2)	E	Tilting pyridine ring
11	734	735.2	—	751.84	Deg. (2)	E	Wagging C–H bond at the ethyl group
12	965	957.2, 957.4	966	961.8, 963.7	Deg. (2)	E	Antisym. pyrazole ring breathing
13	1017	1018.6	1016	991.1	Deg. (2)	E	Sym. pyridine ring breathing
14	1045	1030.6	1045	996.4	Non-Deg.	B_2	Antisym. pyridine ring breathing
15	1057	1057.5	1057	1058.1	Non-Deg.	A_1	Sym. pyridine C–C stretching breathing
16	—	1072.8, 1072.9	1074	1076.1, 1076.8	Deg. (2)	E	Antisym. pyrazole ring breathing
17	1140	1140.4, 1140.5	1145	1149.5, 1149.6	Deg. (2)	E	Antisym. and sym. pyridine ring breathing
18	1160	1194.9	—	1183.4	Non-Deg.	A_1	Sym. pyridine ring breathing
19	—	1205.3, 1205.4	1215	1198.1, 1198.2	Deg. (2)	E	Antisym. and sym. pyrazole tilting, H–C rocking

Table 2 Same as Table 1 for vibrational modes between 1222 cm^{-1} up to 1737 cm^{-1}

	Vibrational modes in [cm^{-1}]						
No.	LS_{exp}	LS_{calc}	HS_{exp}	HS_{calc}	Deg.	Sym.	Description
20	1223	1222.1, 1223.6	1223	1220.9, 1227.9	Deg (2)	E	Ethyl group rocking, C–C stretching near the ethyl group
21	1262	1258.0	1262	1262.7	Non-Deg	A_1	Breathing N–N pyrazole mode, sym. C–N stretching
22	1287	1258.9	1286	1264.3	Non-Deg	B_2	N–N pyrazole ring breathing, antisym. C–N stretching
23	1303	1322.6	1301	1317.9, 1318.2	Deg (2)	E	Antisym. and sym. pyrazole ring breathing
24	1338	1336.8	—	1340.6, 1342.4	Deg (2)	E	Tilting pyridine ring
25	1378	1373.2, 1373.3	1379	1373.0, 1373.2	Deg (2)	E	Wagging H–C bond at the ethyl group
26	—	1409.9	—	1404.8	Non-Deg	A_2	Pyridine tilting
27	1412	1410.0, 1410.4, 1413.0, 1415.5	1404	1407.1, 1409.3, 1411.5, 1415.1	Deg (4)	—	Pyridine ring breathing
28	1442	1441.6, 1457.6	1440	1441.4, 1441.5, 1457.3, 1457.4	Deg (4)	—	Tilting functional group
29	1472	1465.6	1462	1467.0	Deg (3)	—	Light pyridine ring breathing mode
30	1502	1504.8	1500	1466.3, 1467.0	Deg (2)	E	Sym. pyridine C–C bending
31	1526	1547.2, 1547.3	1528	1554.2, 1555.9	Non-Deg	A_1	Pyridine ring stretching
32	1576	1599.6	1584	1589.0, 1589.3	Deg (2)	E	Antisym. and sym. C–C pyridine stretching
33	1631	1602.8, 1627.1	1631	1626.2, 1630.0	Deg (2)	E	Antisym. and sym. C–C pyridine stretching
34	1730	1720.4, 1720.6	1737	1720.8, 1721.3	Deg (4)	—	Antisym. and sym. O–C stretching

We note that vibrational modes can be assigned to general categories, such as tilting of the ligands and pyridine/pyrazole breathing modes, and to molecule-specific categories, such as iron modes (*e.g.*, Fe–N stretching, Fe-ligand bending), special rocking modes of the ligands, ethyl group vibrations (*e.g.*, CH_3 rocking, CH_2 wagging), and carbonyl (CO) stretching.

Inspecting the data in Table 1, we identify a group of modes, labeled 6, centered around 310 cm^{-1} in the LS state and around 296 cm^{-1} in the HS state. These modes correspond to Fe motion within the nearly octahedral cage formed by the N atoms. While an ideal octahedron would exhibit three-fold degeneracy, the calculations find a splitting of 10 cm^{-1} in LS and more than 20 cm^{-1} in the HS state, indicating a stronger deformation of the octahedral bonding environment in the HS state. Moreover, these vibrational modes are softer in the HS state, consistent with a more spacious cage and elongated Fe–N bonds. We note that other low-lying modes, particularly mode 4, also contain smaller contributions of Fe displacement. This can be understood from the requirement for a conserved center of mass of the whole complex, which necessitates Fe motion when the ligands have different displacement amplitudes. From the experimental perspective, it is important to realize that modes 4 and 6, involving Fe motion, appear as only relatively small peaks. The weak change in dynamic dipole moment for these modes results in weak Raman activity, limiting their usefulness as a fingerprint of the spin state.

The vibrational spectra of the HS and LS states exhibit distinct features of spin crossover-induced structural and

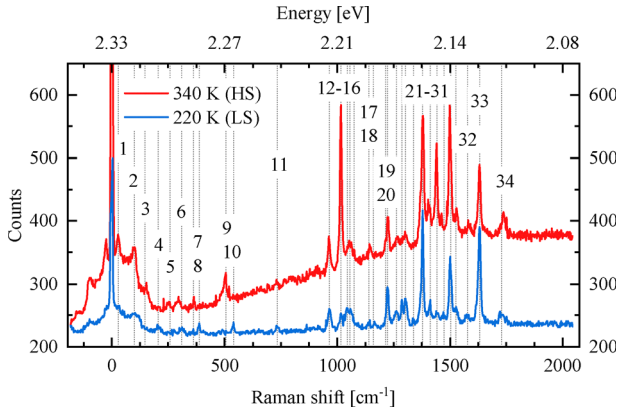

Fig. 4 Detailed Raman spectra at two different temperatures: 220 K (blue) and 340 K (red). The dashed lines label the vibrational modes listed in the Tables 1 and 2.

Table 3 Average velocities of the domain fronts for heating and cooling at different temperature rates of the different *in situ* videos

Temperature rate [K min^{-1}]	Average velocity (heating) [μm s^{-1}]	Average velocity (cooling) [μm s^{-1}]
5	35.60 ± 0.8	18.26 ± 8.88
10	—	59.36 ± 12.68
15	110.00 ± 31.22	45.65 ± 21.67

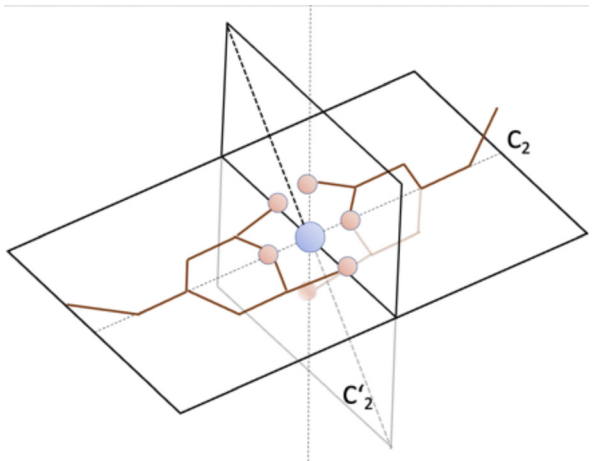

Fig. 5 Schematic illustrating the D_{2d} symmetry of the complex formed by the Fe atom (blue sphere) and its attached N atoms (brown spheres). Two-fold rotation axes are marked by C_2 and C_2'. Mirroring by one of the indicated planes followed by a 90° rotation also maps the complex onto itself.

electronic changes. Modes involving direct iron-ligand interactions show significant shifts, such as mode 7 (asymmetric N–Fe stretching), which redshifts by 72 cm^{-1} (LS: 361 cm^{-1} → HS: 289 cm^{-1}), reflecting stronger N–Fe bonds in the LS state. Similarly, mode 8 (N–Fe stretching) shifts from 387 cm^{-1} (LS) to 336.0 cm^{-1} (HS), consistent with bond softening. In contrast, ligand-dominated vibrations, like mode 15 (symmetrical pyridine C–C stretching), remain nearly unchanged (LS: 1057 cm^{-1} → HS: 1058.1 cm^{-1}), indicating their insensitivity to spin state. The gaps in the spectra are also indicative of spin state: mode 4 (iron-linked tilting) is unobserved in HS, suggesting HS rigidity, while mode 9 (pyridine tilting) is not detected in the LS data, likely due to symmetry or intensity shifts.

3.2.2. Iron-sensitive mode range. Iron-sensitive modes highlight coordination changes. Mode 3 (147 cm^{-1} in LS) arises from Fe geometry rearrangement, while mode 6 (C–N bending) splits into three peaks in HS (279.8–288.0 cm^{-1}) compared to three clustered LS peaks (308.7–315.8 cm^{-1}), signaling symmetry reduction. Ligand dynamics also differ: ethyl group tilting (mode 5) splits into two HS peaks (261.9–262.3 cm^{-1}), and pyrazole breathing (mode 12, Fig. 6, middle row) weakens slightly in HS (HS 961.8–963.7 cm^{-1} → LS: 957.2–957.4 cm^{-1}) well established in literature.[33,34,36,51]

We note that pairs of modes that would be degenerate in an idealized D_{2d}-symmetric complex may show detectable splitting depending on structural distortions. While such splitting remains below the detection limit in mode 19 (pyrazole tilting), mode 20 (ethyl rocking) shifts frequencies (LS: 1223 cm^{-1} → HS: 1220.9–1227.9 cm^{-1}) and, according to the calculations, increases its splitting in the HS state. Notably, Raman activity depends on mode symmetry. Non-degenerate A_1 or B_2 modes (*e.g.*, modes 14 or 15) are usually Raman-active while modes with symmetries like A_2 (*e.g.*, mode 26) can be Raman-inactive according to molecule symmetry. This explains why some modes are experimentally more intense or less intense in Raman spectra.

These trends show that LS strengthens metal–ligand bonds while imposing steric constraints on the ligands (*e.g.*, the ethyl group swing in mode 11 shifts from 735 cm^{-1} to 751.9 cm^{-1}). Persistent pyridine ring vibrations (*e.g.*, modes 13–15) confirm aromatic rigidity, whereas pyrazole modes are more spin-sensitive due to their aromaticity (see ref. 52). The interplay between symmetry-governed Raman activity and spin-state-dependent frequency shifts provides a dual criterion for distinguishing HS from LS configurations. The data offer a mechanistic framework for spin-state transitions, linking vibrational signatures to structural rearrangements critical for functional spin-crossover materials.

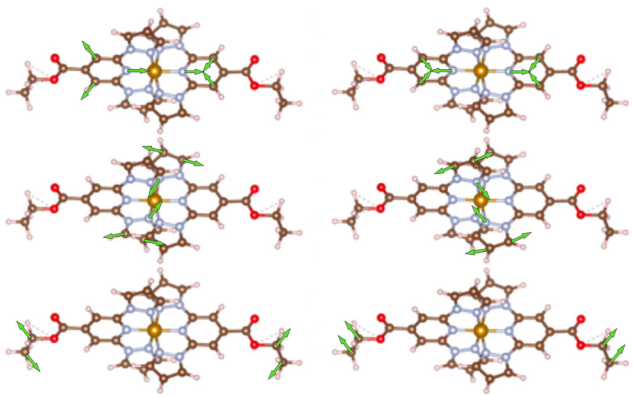

Fig. 6 Visualization of selected Raman modes, top row: antisymmetric and symmetric pyridine breathing (13/14); middle row: antisymmetric and symmetric pyrazole ring breathing (12); bottom row: ethyl group modes.

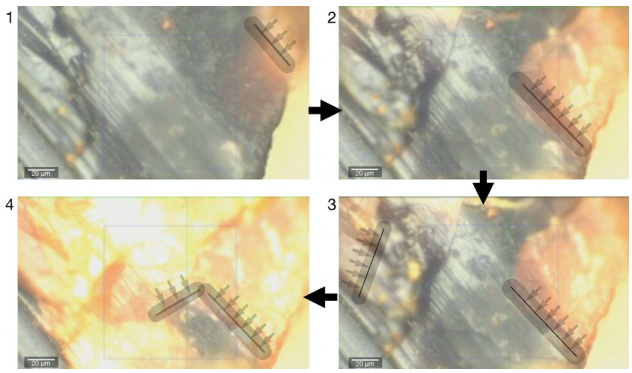

Fig. 7 Optical image (size W: 220 μm × H: 130 μm) of the crystal taken by an optical microscope after heating with a heat rate of 5 K min^{-1} from 300 K to 318 K, the area or averaged linearized frontier of the transition is shown in gray boxes and with a black line. The direction of movement of the front is also indicated by arrows.

3.2.3 Medium-mode range. Next, we turn to higher-lying vibrations beyond the breathing modes. Experimentally determined vibrational frequencies for these modes span the range from 1223 cm^{-1} (mode 20) to 1730 cm^{-1} (mode 34). A comparison with calculated harmonic frequencies reveals good agreement, as exemplified by mode 21 (1262 cm^{-1} experimental *vs.* 1258.0 cm^{-1} calculated). However, some deviations are also observed, such as in mode 23 (1303 cm^{-1} experimental *vs.* 1322.6 cm^{-1} calculated), which may be attributed to the limitations of the harmonic approximation. Furthermore, some modes that appear as a single peak in the measured spectra, such as mode 27 (1410.0 cm^{-1}, 1415.5 cm^{-1} calculated), exhibit a splitting in the calculated frequencies, suggesting a subtle symmetry reduction or vibrational coupling. Experimentally, modes 24 and 26 were not detected, possibly due to weak Raman activity or overly large spectral broadening.

3.2.4 Higher-mode range. The characterization of vibrational motions reveals that lower-frequency modes (21–25) are predominantly pyrazole ring deformations, including symmetric and asymmetric N–N stretching (modes 21 and 22), with mode 25 involving ethyl group H–C wagging. Mid-frequency modes (26–30) include pyridine ring tilting (mode 26) and mixed C–C/N–C motions, such as symmetric pyridine bending (mode 30). Higher-frequency modes (31–34) are dominated by pyridine ring stretching (modes 31–33) and O–C stretching (mode 34), with an undetected splitting in mode 33 (∼1630 cm^{-1}, C–C stretching) reflecting antisymmetric *versus* symmetric displacements in the two ligands.

Key observations include the prevalence of pyridine-dominated modes at higher frequencies (>1338 cm^{-1}) indicating stronger C–C bonds in the six-membered ring and the agreement between experimental and calculated frequencies for stretching-dominated vibrations like mode 31 (1526 cm^{-1} experimental *vs.* 1547.2 cm^{-1} calculated), validating our computational method for these motions. Overall, the vibrational signatures reflect the molecular structure and symmetry, highlighting the conformational complexity arising from the coupling of pyridine/pyrazole motions and ethyl group dynamics.

3.2.5. Thermochemical analysis. Knowledge of the vibrational frequencies enables us to estimate within the harmonic approximation the contribution of free energy at finite temperature to the relative stability of LS and HS states. Since the vibrations in the HS state are mostly softer, the free energy of vibrations at T = 300 K help to stabilize the HS state by about 0.20 eV. This resonates with the experimentally observed trend of a transition to the HS state at higher temperatures. In principle, one may attempt to give a theoretical estimate of the switching temperature, but the limited accuracy of DFT methods in obtaining the electronic ground state energy makes this unfeasible at present. The PBE functional used by us renders at T = 0 K the LS more stable than the HS state by 0.55 eV, and hence switching near room temperature would not be expected. Single-energy-point calculations with the B3LYP functional gave only 0.15 eV for this energy difference, and adding the vibrational correction of 0.20 eV thus makes the HS state thermodynamically more favorable at room temperature. An accurate estimation of the switching temperatures can only be done with a more reliable DFT functional for Fe complexes becoming available in the future.

3.3 Motion of the phase boundaries

Next, we turn to the dynamical aspects of the LS-HS transition in polycrystalline samples. The dynamic spin-state transition within the SCO crystal was meticulously examined through *in situ* optical microscopy and subsequent video analysis, under controlled thermal heat flow. This investigation aimed to elucidate the mechanisms governing the hysteretic spin-state switching, as evidenced by observed morphological and chromatic alterations and the quantified propagation velocity of the transition front. Upon heating from 300 K to 318 K at a rate of 5 K min^{-1}, the SCO crystal underwent a transformation from a grayish-brown to an orange hue, concurrent with the initiation of micro-fracturing. Further elevation of temperature to 340 K intensified this chromatic transition.

Conversely, cooling back to 300 K yielded no discernible changes, confirming the material's inherent hysteretic behavior. Subsequent cooling to 220 K induced further micro-fracturing and the grayish-brown coloration returned, signifying the recovery of the LS state. Comparative analysis of the initial LS state at 300 K with the post-thermal cycle LS state at 200 K revealed substantial modifications in crystal morphology, consistent with the previously documented "self-grinding" phenomenon.[35]

Video microscopy, coupled with linear interpolation of the transition front, allowed for the quantification of the HS to LS transition propagation velocity. During heating from 300 K to 318 K at 5 K min^{-1}, the propagation velocity was determined to be 35.6 ± 0.8 μm s^{-1} (*cf.* Fig. 3) equivalent to (36.5 ± 0.8) × 10^3 molecular diameters per second, assuming a homogeneous molecular volume of 992.83 $Å^3$ per complex. This implies that a row of switched complexes gets attached to an existing domain within 27.3 μs on average.

This observed velocity exceeds previously reported values[53–62] even by one order of magnitude, see *e.g.* ref. 59,62. This is

tentatively attributed to intrinsic material properties, such as the broad thermal hysteresis and extrinsic factors, including the high heating rate. Increased heating rates further amplified the propagation velocity. Isothermal analysis at 318 K post-heating yielded similar velocities (31 ± 4 μm s^{-1}). The reverse process, passive cooling, resulted in a propagation velocity of (18 ± 9 μm s^{-1}), corresponding to a molecular interaction velocity of $(18 \pm 9) \times 10^3$ molecular diameters per second.

Increased cooling rates also resulted in higher propagation velocities. The observed disparity in propagation velocities between heating and cooling is attributed to structural changes, variations in Fe–N bond lengths, and micro-fractures, which introduce strain and impede transition front propagation. Micro-fractures and cracks were observed to impede the transition front, leading to pinning effects, which were accounted for in velocity determinations. However, we could not confirm a systematic reduction of the velocity from one heating cycle to the next. The high propagation velocities observed during heating suggest a rapid spin-state transition, influenced by the broad thermal hysteresis and heating rate.

The observed colorimetric variations stem from changes of the electronic structure of the complexes induced by spin-state transitions. Specifically, the observed color can be explained as combined effects of d–d electronic transitions, charge transfer transitions, and alterations in ligand field strength. As has been shown for a different complex,[22] the core mechanism hinges on the change in the energy difference (10 *Dq*) between the Fe(II) ion's 3d orbitals during spin-state transitions, which directly affects d–d electronic transitions and subsequently the absorption spectrum, leading to visible color changes.

Conclusions

This paper investigated the structural and dynamic changes accompanying the spin transition from the low-spin to the high-spin state. Key findings reveal that this transition involves alterations in cellular morphology and a 2% volume increase, exhibiting hysteretic behavior with optically distinguishable phase coexistence. Kinetic analysis of the LS/HS domain boundary velocity within the hysteresis loop provided insights into the switching dynamics. While optical microscopy elucidated macroscopic and mesoscopic strain effects on crystal integrity, Raman spectroscopy probed sub-molecular dynamics and interactions. Distinct Raman bands showed significant intensity and frequency variations correlating with the transition between the low-spin and high-spin states, providing key vibrational signatures of this electronic change. Combined with first-principles calculations, Raman spectroscopy provided a detailed mode assignment, establishing a spectral fingerprint of the spin-state transition. A general downward frequency shift was observed in iron-based modes, revealing bond weakening (softening) during the HS state's approximately 10% bond elongation. Moreover, analysis of video microscopy images enabled the determination of the propagation velocity of phase domain boundaries. Distinct average velocities during heating and cooling, depending on the rate of temperature change, were found. For the present SCO complex, the absolute values were in the range of tens of μm s^{-1}, and thus about an order of magnitude larger than previously reported values for other SCO complexes. In summary, the paper demonstrates characteristic spectral features for the LS and HS states, primarily defined by a general downward frequency shift, with some modes exhibiting dominant intensity variations.

Conflicts of interest

There are no conflicts to declare.

Data availability

Data for this article, including videos are available at https://uni-duisburg-essen.sciebo.de/s/Ib18Asdp2ewsrUX.

Acknowledgements

G. K., L. K., S. S., M. S., H. W., and P. K. gratefully acknowledge the funding by the Deutsche Forschungsgemeinschaft (DFG, German Research Foundation) – Project-ID 278162697 – SFB 1242, projects A05, B02, and C05. S. S. and M. S. acknowledge financial support by the Deutsche Forschungsgemeinschaft (DFG, German Research Foundation) – Project-ID 429784087. G. K. and P. K. gratefully acknowledge the computing time granted by the Center for Computational Sciences and Simulation (CCSS) of the University of Duisburg-Essen and provided on the supercomputer magnitUDE (DFG Grant No. INST 20876/209-1 FUGG and INST 20876/243-1 FUGG) at the Zentrum für Informations- und Mediendienste (ZIM).

References

1 T. Kitazawa, *Crystals*, 2019, **9**, 382.
2 P. Gütlich, Y. Garcia and H. A. Goodwin, *Chem. Soc. Rev.*, 2000, **29**, 419–427.
3 C. Lefter, S. Rat, J. S. Costa, M. D. Manrique-Juarez, C. M. Quintero, L. Salmon, I. Seguy, T. Leichle, L. Nicu, P. Demont, A. Rotaru, G. Molnar and A. Bousseksou, *Adv. Mater.*, 2016, **28**, 7508–7514.
4 C. Bartual-Murgui, A. Akou, C. Thibault, G. MolnÃ¡r, C. Vieu, L. Salmon and A. Bousseksou, *J. Mater. Chem. C*, 2015, **3**, 1277–1285.
5 Y. Guo, S. Xue, M. M. Dirtu and Y. Garcia, *J. Mater. Chem. C*, 2018, **6**, 3895–3900.
6 W. Li, A. Rotaru, M. Wolff, S. Demeshko, F. Meyer and Y. Garcia, *J. Mater. Chem. C*, 2023, **11**, 11175–11184.
7 E. Resines-Urien, E. Fernandez-Bartolome, A. Martinez-Martinez, A. Gamonal, L. Pineiro-Lopez and J. S. Costa, *Chem. Soc. Rev.*, 2023, **52**, 705–727.
8 O. Kahn, J. Kröber and C. Jay, *Adv. Mater.*, 1992, **4**, 718–728.

9 S. K. Kuppusamy, L. Spieker, B. Heinrich, H. Wende and M. Ruben, *ChemRxiv*, 2022, preprint, DOI: 10.26434/chemrxiv-2022-mnh4n.
10 L. Kämmerer, G. Kämmerer, M. Gruber, J. Grunwald, T. Lojewski, L. Mercadier, L. Le Guyader, R. Carley, C. Carinan, N. Gerasimova, D. Hickin, B. E. Van Kuiken, G. Mercurio, M. Teichmann, S. K. Kuppusamy, A. Scherz, M. Ruben, K. Sokolowski-Tinten, A. Eschenlohr, K. Ollefs, C. Schmitz-Antoniak, F. Tuczek, P. Kratzer, U. Bovensiepen and H. Wende, *ACS Nano*, 2024, **18**, 34596–34605.
11 B. Weber, W. Bauer and J. Obel, *Angew. Chem., Int. Ed.*, 2008, **47**, 10098–10101.
12 M. Fumanal, F. Jiménez-Gravalos, J. Ribas-Arino and S. Vela, *Inorg. Chem.*, 2017, **56**, 4474–4483.
13 O. Iasco, E. Riviere, R. Guillot, M. Buron-Le Cointe, J.-F. Meunier, A. Bousseksou and M.-L. Boillot, *Inorg. Chem.*, 2015, **54**, 1791–1799.
14 A. Kaiba, H. J. Shepherd, D. Fedaoui, P. Rosa, A. E. Goeta, N. Rebbani, J. F. Letard and P. Guionneau, *Dalton Trans.*, 2010, **39**, 2910–2918.
15 K. Takahashi, *Inorganics*, 2018, **6**, 1–4.
16 J. G. Park, I.-R. Jeon and T. D. Harris, *Inorg. Chem.*, 2015, **54**, 359–369.
17 A. Arroyave, A. Lennartson, A. Dragulescu-Andrasi, K. S. Pedersen, S. Piligkos, S. A. Stoian, S. M. Greer, C. Pak, O. Hietsoi, H. Phan, S. Hill, C. J. McKenzie and M. Shatruk, *Inorg. Chem.*, 2016, **55**, 5904–5913.
18 S. K. Kuppusamy, A. Mizuno, L. Kammerer, S. Salamon, B. Heinrich, C. Bailly, I. Salitros, H. Wende and M. Ruben, *Dalton Trans.*, 2024, **53**, 10851–10865.
19 K. Senthil Kumar, B. Heinrich, S. Vela, E. Moreno-Pineda, C. Bailly and M. Ruben, *Dalton Trans.*, 2019, **48**, 3825–3830.
20 H. Hagiwara, T. Masuda, T. Ohno, M. Suzuki, T. Udagawa and K. I. Murai, *Cryst. Growth Des.*, 2017, **17**, 6006–6019.
21 M. A. Halcrow, *Chem. Lett.*, 2014, **43**, 1178–1188.
22 C. Lochenie, K. Schötz, F. Panzer, H. Kurz, B. Maier, F. Puchtler, S. Agarwal, A. Köhler and B. Weber, *J. Am. Chem. Soc.*, 2018, **140**, 700–709.
23 J.-H. Yang, Y.-X. Zhao, J.-P. Xue, Z.-S. Yao and J. Tao, *Inorg. Chem.*, 2021, **60**, 7337–7344.
24 S. Ossinger, L. Kipgen, H. Naggert, M. Bernien, A. J. Britton, F. Nickel, L. M. Arruda, I. Kumberg, T. A. Engesser, E. Golias, C. Nather, F. Tuczek and W. Kuch, *J. Phys.: Condens. Matter*, 2019, **32**, 114003.
25 T. Q. Hung, F. Terki, S. Kamara, M. Dehbaoui, S. Charar, B. Sinha, C. Kim, P. Gandit, I. A. Gural'skiy, G. Molnar, L. Salmon, H. J. Shepherd and A. Bousseksou, *Angew. Chem., Int. Ed.*, 2013, **52**, 1185–1188.
26 L. Poggini, M. Gonidec, J. H. Gonzalez-Estefan, G. Pecastaings, B. Gobaut and P. Rosa, *Adv. Electron. Mater.*, 2018, **4**, 1800204.
27 A. C. Bas, X. Thompson, L. Salmon, C. Thibault, G. Molnár, O. Palamarciuc, L. Routaboul and A. Bousseksou, *Magnetochemistry*, 2019, **5**, 1–14.
28 M. Matsuda, K. Kiyoshima, R. Uchida, N. Kinoshita and H. Tajima, *Thin Solid Films*, 2013, **531**, 451–453.
29 W. Gawelda, A. Cannizzo, V. T. Pham, F. V. Mourik, C. Bressler and M. Chergui, *J. Am. Chem. Soc.*, 2007, **129**, 8199–8206.
30 N. Huse, H. Cho, K. Hong, L. Jamula, F. M. D. Groot, T. K. Kim, J. K. McCusker and R. W. Schoenlein, *J. Phys. Chem. Lett.*, 2011, **2**, 880–884.
31 J. E. Monat and J. K. McCusker, *J. Am. Chem. Soc.*, 2000, **122**, 4092–4097.
32 H. T. Lemke, K. S. Kjær, R. Hartsock, T. B. V. Driel, M. Chollet, J. M. Glownia, S. Song, D. Zhu, E. Pace, S. F. Matar, M. M. Nielsen, M. Benfatto, K. J. Gaffney, E. Collet and M. Cammarata, *Nat. Commun.*, 2017, **8**, 15342.
33 M. Cavallini, I. Bergenti, S. Milita, J. C. Kengne, D. Gentili, G. Ruani, I. Salitros, V. Meded and M. Ruben, *Langmuir*, 2011, **27**, 4076–4081.
34 N. Suryadevara, A. Mizuno, L. Spieker, S. Salamon, S. Sleziona, A. Maas, E. Pollmann, B. Heinrich, M. Schleberger, H. Wende, S. K. Kuppusamy and M. Ruben, *Chem. – A Eur. J.*, 2021, **28**, e202103853.
35 Y. Miyazaki, T. Nakamoto, S. Ikeuchi, K. Saito, A. Inaba, M. Sorai, T. Tojo, T. Atake, G. S. Matouzenko, S. Zein and S. A. Borshch, *J. Phys. Chem. B*, 2007, **111**, 12508–12517.
36 E. J. Devid, P. N. Martinho, M. V. Kamalakar, I. Salitros, U. Prendergast, J.-F. Dayen, V. Meded, T. Lemma, R. González-Prieto, F. Evers, T. E. Keyes, M. Ruben, B. Doudin and S. J. van der Molen, *ACS Nano*, 2015, **9**, 4496–4507.
37 S. Rackwitz, J. A. Wolny, K. Muffler, K. Achterhold, R. Rüffer, Y. Garcia, R. Diller and V. Schünemann, *Phys. Chem. Chem. Phys.*, 2012, **14**, 14650–14660.
38 S. Ossinger, H. Naggert, E. Bill, C. Nather and F. Tuczek, *Inorg. Chem.*, 2019, **58**, 12873–12887.
39 J. A. Wolny, S. Rackwitz, K. Achterhold, Y. Garcia, K. Muffler, A. D. Naik and V. Schünemann, *Phys. Chem. Chem. Phys.*, 2010, **12**, 14782–14788.
40 J. A. Wolny, R. Diller and V. Schünemann, *Eur. J. Inorg. Chem.*, 2012, 2635–2648.
41 J.-L. Wang, Q. Liu, X.-J. Lv, R.-L. Wang, C.-Y. Duan and T. Liu, *Dalton Trans.*, 2016, **45**, 18552–18558.
42 J. Diaz-Escobar and V. Kober, *Applications of Digital Image Processing XXXIX*, 2016, p. 99712A.
43 J. P. Perdew, K. Burke and M. Ernzerhof, *Phys. Rev. Lett.*, 1996, **77**, 3865–3868.
44 D. Gentili, F. Liscio, N. Demitri, B. Schäfer, F. Borgatti, P. Torelli, B. Gobaut, G. Panaccione, G. Rossi, A. D. Esposti, M. Gazzano, S. Milita, I. Bergenti, G. Ruani, I. Šalitroš, M. Ruben and M. Cavallini, *Dalton Trans.*, 2016, **45**, 134–143.
45 V. Blum, R. Gehrke, F. Hanke, P. Havu, V. Havu, X. Ren, K. Reuter and M. Scheffler, *Comput. Phys. Commun.*, 2009, **180**, 2175–2196.
46 A. Tkatchenko and M. Scheffler, *Phys. Rev. Lett.*, 2009, **102**, 073005.
47 E. van Lenthe, E. J. Baerends and J. G. Snijders, *J. Chem. Phys.*, 1994, **101**, 9783–9792.
48 S. Sangeetha, V. A. Danie, N. S. F. Nirmal, T. Alwin and T. F. A. Fen, *J. Res. Sci.*, 2014, **2**, 2278–9073.

49 L. M. Lawson Daku, *Phys. Chem. Chem. Phys.*, 2018, **20**, 6236–6253.
50 M. Ester, H.-P. Kriegel, J. Sander and X. Xu, Proceedings of the Second International Conference on Knowledge Discovery and Data Mining, 1996, 226–231.
51 A. Abhervé, M. J. Recio-Carretero, M. López-Jordá, J. M. Clemente-Juan, J. Canet-Ferrer, A. Cantarero, M. Clemente-León and E. Coronado, *Inorg. Chem.*, 2016, **55**, 9361–9367.
52 W.-X. Liu, Z. Yang, Z. Qiao, L. Zhang, N. Zhao, S. Luo and J. Xu, *Nat. Commun.*, 2019, **10**, 4753.
53 F. Varret, C. Chong, A. Slimani, D. Garrot, Y. Garcia and A. D. Naik, *Real-Time Observation of Spin-Transitions by Optical Microscopy*, John Wiley & Sons, Ltd, 2013, ch. 16, pp. 425–441.
54 S. Bonnet, G. Molnár, J. S. Costa, M. A. Siegler, A. L. Spek, A. Bousseksou, W. T. Fu, P. Gamez and J. Reedijk, *Chem. Mater.*, 2009, **21**, 1123–1136.
55 C. Chong, H. Mishra, K. Boukheddaden, S. Denise, G. Bouchez, E. Collet, J. C. Ameline, A. D. Naik, Y. Garcia and F. Varret, *J. Phys. Chem. B*, 2010, **114**, 1975–1984.
56 C. Chong, A. Slimani, F. Varret, K. Boukheddaden, E. Collet, J. C. Ameline, R. Bronisz and A. Hauser, *Chem. Phys. Lett.*, 2011, **504**, 29–33.
57 M. Sy, D. Garrot, A. Slimani, M. Páez-Espejo, F. Varret and K. Boukheddaden, *Angew. Chem., Int. Ed.*, 2016, **55**, 1755–1759.
58 A. Slimani, F. Varret, K. Boukheddaden, C. Chong, H. Mishra, J. Haasnoot and S. Pillet, *Phys. Rev. B:Condens. Matter Mater. Phys.*, 2011, **84**, 1–8.
59 H. Fourati, E. Milin, A. Slimani, G. Chastanet, Y. Abid, S. Triki and K. Boukheddaden, *Phys. Chem. Chem. Phys.*, 2018, **20**, 10142–10154.
60 M. Sy, R. Traiche, H. Fourati, Y. Singh, F. Varret and K. Boukheddaden, *J. Phys. Chem. C*, 2018, **122**, 20952–20962.
61 A. Goujon, F. Varret, K. Boukheddaden, C. Chong, J. Jefti, Y. Garcia, A. D. Naik, J. C. Ameline and E. Collet, *Inorg. Chim. Acta*, 2008, **361**, 4055–4064.
62 R. Traiche, M. Sy, H. Oubouchou, G. Bouchez, F. Varret and K. Boukheddaden, *J. Phys.Chem. C*, 2017, **121**, 11700–11708.